Volume 12 Number 2 14 January 2024 Pages 279-542

Journal of **Materials Chemistry B**

Materials for biology and medicine

rsc.li/materials-b



ISSN 2050-750X



PAPER

Rudy L. Luck, Haiying Liu et al. Sensitive monitoring of NAD(P)H levels within cancer cells using mitochondria-targeted near-infrared cyanine dyes with optimized electron-withdrawing acceptors

Journal of Materials Chemistry B



View Article Online PAPER



Cite this: J. Mater. Chem. B, 2024, 12, 448

Sensitive monitoring of NAD(P)H levels within cancer cells using mitochondria-targeted near-infrared cyanine dyes with optimized electron-withdrawing acceptors†

Dilka Liyana Arachchige, ab Sushil K. Dwivedi, ab May Waters, ab Sophia Jaeger, ab Joe Peters, ab Daniel R. Tucker, Micaela Geborkoff, Thomas Werner, Rudy L. Luck, *\omega *\dag{a} Bhaskar Godugu dand Haiying Liu *\omega *\dag{a} to *\omega *\dag{a} to *\omega *\dag{a} to *\omega *\o

A series of near-infrared fluorescent probes, labeled A to E, were developed by combining electron-rich thiophene and 3,4-ethylenedioxythiophene bridges with 3-quinolinium and various electron deficient groups, enabling the sensing of NAD(P)H. Probes A and B exhibit absorptions and emissions in the nearinfrared range, offering advantages such as minimal interference from autofluorescence, negligible photo impairment in cells and tissues, and exceptional tissue penetration. These probes show negligible fluorescence when NADH is not present, and their absorption maxima are at 438 nm and 470 nm, respectively. In contrast, probes C-E feature absorption maxima at 450, 334 and 581 nm, respectively. Added NADH triggers the transformation of the electron-deficient 3-quinolinium units into electron-rich 1,4-dihydroquinoline units resulting in fluorescence responses which were established at 748, 730, 575, 625 and 661 for probes AH-EH, respectively, at detection limits of 0.15 μM and 0.07 μM for probes A and B, respectively. Optimized geometries based on theoretical calculations reveal non-planar geometries for probes A-E due to twisting of the 3-quinolinium and benzothiazolium units bonded to the central thiophene group, which all attain planarity upon addition of hydride resulting in absorption and fluorescence in the near-IR region for probes AH and BH in contrast to probes CH-EH which depict fluorescence in the visible range. Probe A has been successfully employed to monitor NAD(P)H levels in glycolysis and specific mitochondrial targeting. Furthermore, it has been used to assess the influence of lactate and pyruvate on the levels of NAD(P)H, to explore how hypoxia in cancer cells can elevate levels of NAD(P)H, and to visualize changes in levels of NAD(P)H under hypoxic conditions with CoCl₂ treatment. Additionally, probe A has facilitated the examination of the potential impact of chemotherapy drugs, namely gemcitabine, camptothecin, and cisplatin, on metabolic processes and energy generation within cancer cells by affecting NAD(P)H levels. Treatment of A549 cancer cells with these drugs has been shown to increase NAD(P)H levels, which may contribute to their anticancer effects ultimately leading to programmed cell death or apoptosis. Moreover, probe A has been successfully employed in monitoring NAD(P)H level changes in D. melanogaster larvae treated with cisplatin.

Received 11th September 2023, Accepted 3rd November 2023

DOI: 10.1039/d3tb02124f

rsc.li/materials-b

Introduction

NADH and NAD(P)H are essential coenzymes that play critical roles in redox processes in eukaryotic cells. NADH participates in various biochemical processes, encompassing the respiratory cascades, cytoplasmic glycolysis, enzyme allostery, posttranslational modifications, and redox reactions with different enzymes.²⁻⁵ In contrast, NAD(P)H is required for several metabolic processes, such as nucleotide and lipid synthesis, as well as antioxidant defense. Both coenzymes are integral to maintaining cellular homeostasis and have connections to diverse disease mechanisms, such as cancer.5-7 Elevated levels of

^a Department of Chemistry, Michigan Technological University, Houghton, MI 49931, USA. E-mail: rluck@mtu.edu, hyliu@mtu.edu

^b Health Research Institute, Michigan Technological University, Houghton, MI 49931 USA

^c Department of Biological Sciences, Michigan Technological University, Houghton, MI 49931, USA

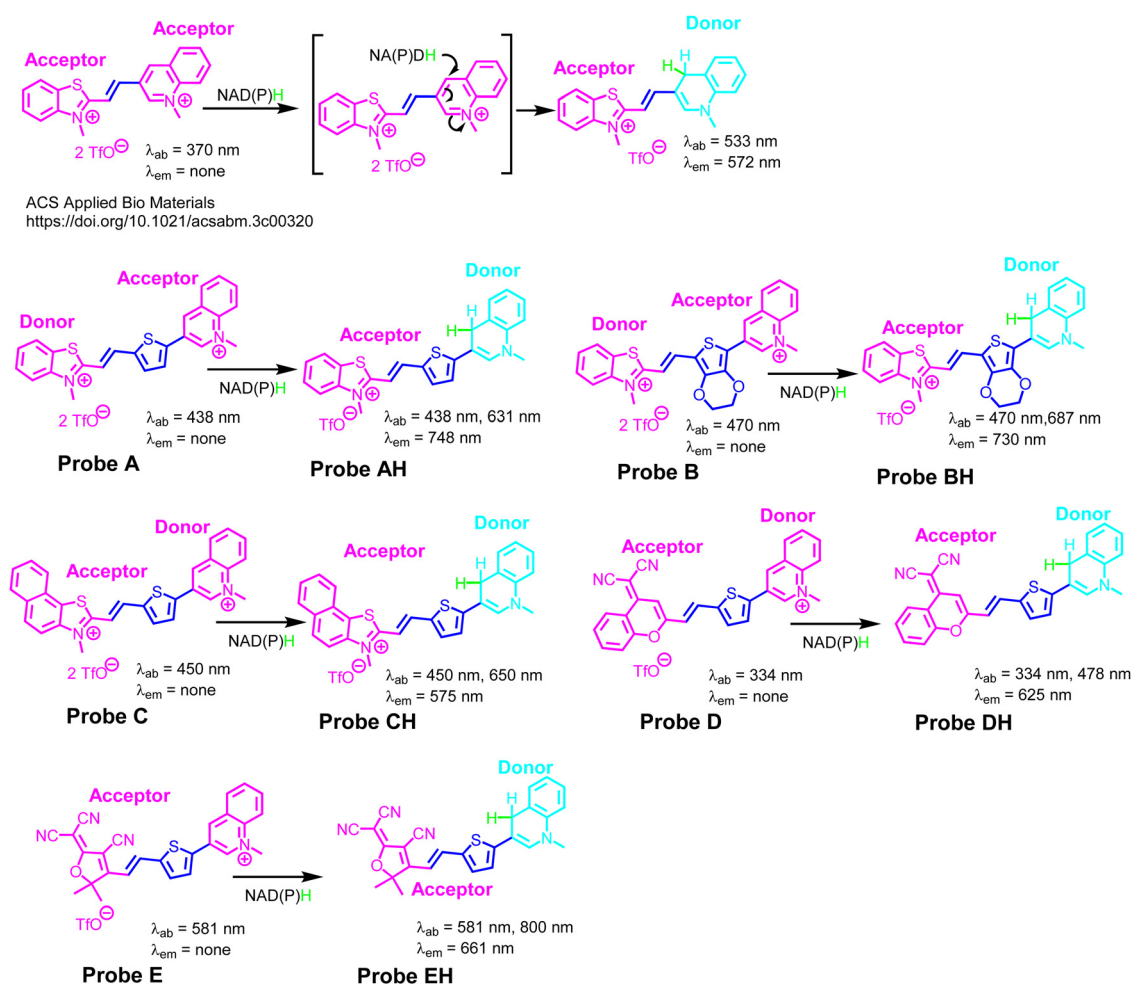
^d Department of Chemistry, University of Pittsburgh, Chevron Science Center, 219 Parkman Avenue, Pittsburgh, PA 15260, USA

[†] Electronic supplementary information (ESI) available: Instrumentation, reagents, synthesis and characterization of the probes, cell imaging, theoretical calculations, and summary of fluorescent probes for NAD(P)H detection. See DOI: https://doi.org/10.1039/d3tb02124f

NADH and NAD(P)H are linked to cancer growth and metastasis, making their detection crucial in developing effective cancer treatments. 5-7 In particular, NAD(P)H plays a crucial role in maintaining redox equilibrium and supporting the high metabolic demand of cancer cells.^{8,9} Several studies have verified that NAD(P)H levels are increased within cancer cells and are associated with tumor growth, invasion, and resistance to therapy.^{8,9} Therefore, detecting NAD(P)H levels in cancer cells can provide valuable information for identifying potential targets for therapy, such as NOX4 or other enzymes participating in NAD(P)H metabolism. Understanding the role of NAD(P)H in cancer cells is essential for developing effective cancer treatments.^{8,9} By measuring NAD(P)H levels, researchers can gain insight into the metabolic pathways and redox balance of cancer cells. This information can help identify potential targets for therapy and develop new drugs that specifically target cancer cells. Hence, detecting NAD(P)H within cancer cells becomes a pivotal stride in devising efficacious cancer therapies. Some methods have been reported to determine NAD(P)H concentrations, but some have limitations such as susceptibility to interference, cell damage, photobleaching, and inadequate specificity.^{5,10} The amalgamation of fluorescent probes with a

confocal fluorescence microscope has surfaced as a potent technique for discerning intracellular NADH and NAD(P)H, presenting numerous benefits. 5,11-25 However, NADH fluorescence can interfere with fluorescent probe imaging, and thus underscoring the importance of formulating fluorescent probes with emission wavelengths significantly exceeding 450 nm.²⁶ Fluorescent probes combined with a confocal fluorescence microscope offer advantages in detecting intracellular NADH and NAD(P)H, but the interference of NADH fluorescence with fluorescent probe imaging necessitates the development of probes with longer emission wavelengths.^{5,11-25} Fluorescent probes emitting in the near-infrared range, spanning from 650 nm to 1700 nm, hold special allure because they can penetrate deeper tissue and cause less photodamage to cells and tissues, resulting in less background autofluorescence interference.27-34

This article delves into the production of two near-infrared cyanine dves, namely probes A and B, designed for NAD(P)H sensing purposes (Scheme 1). We accomplished this by connecting the 3-quinolinium unit to the benzothiazolium unit using thiophene and 3,4-ethylenedioxythiophene linkages with abundant electron density. To investigate the impact of



Scheme 1 Reactions of NAD(P)H with probes A-E. Donor and acceptor labels are based on the current density illustrations in Fig. 5.

electron-withdrawing acceptors on the optical properties of the probes, we synthesized three additional fluorescent probes (probes C, D, and E). These probes were crafted by connecting a 3-quinolinium acceptor to a variety of electron-deficient heterocycles, which included naphtho[2,1-d]thiazolium, 2-(2methyl-4H-chromen-4-ylidene)malononitrile, and 2-(3-cyano-4,5,5-trimethylfuran-2(5H)-ylidene)malononitrile, using a thiophene bridge (Scheme 1). Probes A and B contain primary absorption maxima at 438 nm and 470 nm without exhibiting fluorescence, respectively. Nonetheless, when the 3-quinolinium units within probes A and B undergo reduction by NAD(P)H, transitioning into electron-rich 1-methyl-1,4-dihydroquinoline units, the emission of the probes becomes activated at 748 nm and 730 nm with detection limits of 0.15 µM and 0.07 µM, correspondingly. This arises from the NAD(P)H-induced generation of novel donor- π -acceptor cyanine architectures, leading to fresh absorption maxima at 631 nm and 687 nm, respectively. Employing highly electron-dense thiophene and 3,4-ethylenedioxythiophene linkages has adeptly facilitated the adjustment of both cyanine dyes' absorption and fluorescence to the nearinfrared spectrum, while the probes' substantial Stokes shift will effectively counteract excitation wavelength overlap. In contrast to the non-fluorescent nature of probes C, D, and E in the absence of NADH, the introduction of NADH induced distinct visible fluorescence signals at 575 nm, 625 nm, and 661 nm for each probe, respectively. This demonstrates the crucial importance of selecting suitably optimized electron-withdrawing acceptors to attain effective near-infrared absorption and emission characteristics for the probes. Probe A has demonstrated successful utilization in diverse applications. It has proven to be effective in monitoring glycolysis-induced NAD(P)H levels and targeting mitochondria. Moreover, it has been employed to investigate the impact of lactate and pyruvate on NAD(P)H levels, to examine how hypoxia increases the level of NAD(P)H in cancer cells, and to visualize variances in NAD(P)H levels under hypoxic conditions induced by CoCl₂ treatment. Furthermore, probe A has enabled the investigation into the impact of chemotherapy drugs on metabolic activity and energy dynamics within cancerous cells, particularly gemcitabine, camptothecin, and cisplatin, through modulation of NAD(P)H levels. Furthermore, probe A was efficiently utilized to track fluctuations in NAD(P)H levels during cisplatin treatment in D. melanogaster larvae.

Results and discussion

Synthetic methodology

Probes **A** and **B** were designed to extend the NADH-sensing capabilities of cyanine dyes into the near-infrared range through the integration of bridging units rich in electron density, such as thiophene and 3,4-ethylenedioxythiophene. The process of synthesizing these probes is illustrated in Scheme 2. Firstly, to create probe **A**, 5-bromo-2-thiophenecarboxaldehyde (2) was coupled with 3-quinolineboronic acid (1) using a Suzuki palladium-catalyzed reaction under basic conditions, forming 5-(quinolin-3-yl)thiophene-2-carbaldehyde (3) as an intermediate. ²⁴ Subsequently,

intermediate 3 was coupled with 2,3-dimethylbenzo[d]thiazol-3-ium trifluoromethanesulfonate (4), yielding (E)-3-methyl-2-(2-(5-(quinolin-3-yl)thiophen-2-yl)vinyl)benzo[d]thiazol-3-ium (5), which underwent methylation to form probe A. A parallel synthetic route was employed for probe B, employing 7-bromo-2,3-dihydrothieno[3,4-b][1,4]dioxine-5-carbaldehyde (6) in lieu of 5-bromo-2thiophenecarboxaldehyde (2), mirroring the method applied for probe A's preparation. To investigate the impact of electronwithdrawing acceptors, we synthesized three additional fluorescent probes (probes C, D, and E). These probes were developed by connecting the 3-quinolinium acceptor to three distinct compounds: naphtho[2,1-d]thiazolium, 2-(2-methyl-4H-chromen-4ylidene)malononitrile, and 2-(3-cyano-4,5,5-trimethylfuran-2(5H)ylidene)malononitrile. This was achieved by employing a thiophene bridge, following the same synthetic approach used for probe A, but with the substitution of 2,3-dimethylbenzo[d]thiazol-3-ium trifluoromethanesulfonate (4) with various electron-withdrawing acceptors. The probes were characterized by NMR and highresolution mass spectrometers (Fig. S1-S14, ESI†).

Analysis of optical properties for NADH detection

The optical characteristics of a molecule are heavily influenced by its electronic structure, a factor tightly intertwined with the degree of π -conjugation present within the molecule. π -conjugation entails the dispersion of π -electrons over several atoms within a molecule, frequently through alternating sequences of single and double bonds. The extent of π -conjugation significantly impacts a molecule's optical attributes, as heightened π-conjugation decreases the energy threshold for light absorption, leading to extended absorption wavelengths. When NADH is not present, probe A exhibits a primary absorption peak at 438 nm alongside a markedly faint peak at 631 nm (Fig. 1). Conversely, probe B showcases a 470 nm absorption peak attributed to its heightened electron density conferred by the 3,4-ethylenedioxythiophene linkage. The extended conjugation length enables greater electron delocalization within the molecule, leading to a shift towards longer wavelengths in the absorption spectrum. As NADH concentration gradually rises, both probes A and B experience pronounced absorption enhancements, stemming from the transformation of their electron-deficient 3-quinolinium units into electron-rich 1,4-dihydroquinoline units, a reaction triggered by NADH. This sequence culminates in the creation of precisely structured donor-π-acceptor cyanine architectures, characterized by heightened intramolecular charge transfer from 1,4-dihydroquinoline donors to benzothiazolium acceptors. Consequently, this results in ultimate absorption maxima at 631 nm and 687 nm, as depicted in Fig. 1.

Probes **A** and **B** are tailored for the assessment of NADH concentration alterations via near-infrared fluorescence emission. Notably, probe **A** demonstrates emission at 748 nm, whereas probe **B** showcases emission at 730 nm, as illustrated in Fig. 2. Our results demonstrate that probes **A** and **B** are highly sensitive tools for detecting NADH across a wide dynamic range. Probe **A** provided a linear fluorescent response to varying NADH concentrations from 0 to 35 μ M (Fig. S15, ESI†). Similarly, probe **B** displayed a linear relationship

Scheme 2 Synthetic methods to make probes A, B, C, D and E.

between fluorescence intensity and NADH levels over the range between 0 and 55 μM (Fig. S15, ESI†). These excellent linear correlations highlight the quantitative detection capabilities of

probes A and B in measuring NADH fluctuations. The broad linear ranges indicate that the probes can reliably detect small changes in NADH concentrations, while also remaining

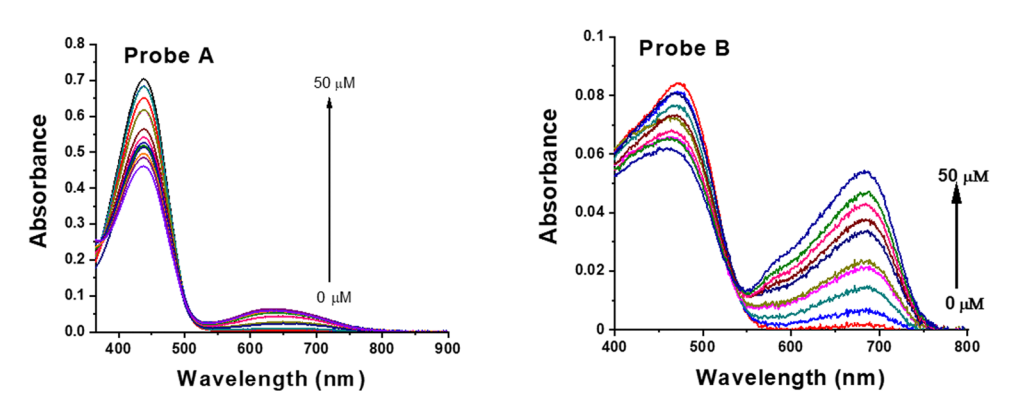


Fig. 1 Absorption profiles of probes A (left) and B (right), each at 10 μM, under varying NADH concentrations, observed after 60-minute and 120-minute incubation times for probe A and probe B respectively. The experiments were conducted in pH 7.4 phosphate buffer containing 10% DMSO.

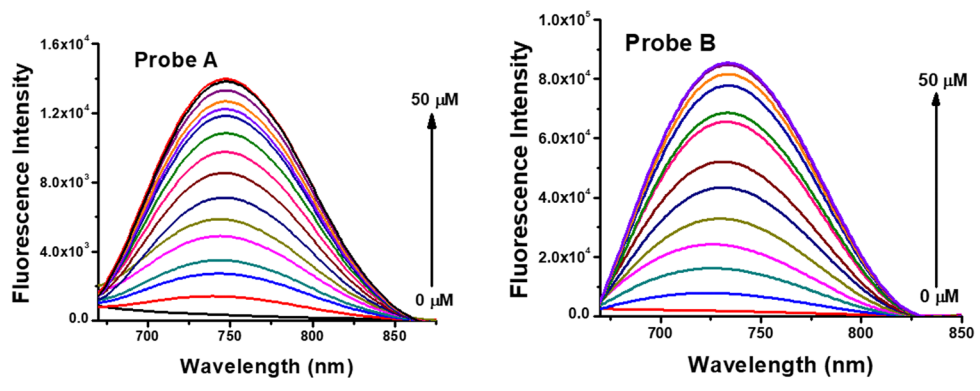


Fig. 2 Emission profiles of probes A (left) and B (right), each at 10 μM, across varying NADH concentrations, observed following 60-minute and 120minute incubation durations for probe A and probe B, respectively. The experiments were conducted under excitation at 630 nm in pH 7.4 phosphate buffer containing 10% DMSO

accurate at higher physiologically relevant NADH levels. Overall, probes A and B exhibit outstanding sensitivity and quantitation, making them valuable tools for investigating NADH dynamics and redox processes. Their robust performance across a wide NADH range demonstrates their significant potential for biological imaging and bioanalysis applications requiring precise NADH detection. Probe A displayed faster response kinetics to NADH, fully reacting within 50 minutes, compared to the 120 minutes required for full activation of probe B (Fig. 3). This more rapid reaction time enables probe A to monitor dynamic changes in NADH levels over shorter timescales. The increased response time in probe B compared to probe A may be attributed to the greater overall stability achieved with the central 2,3-dihydrothieno[3,4-b][1,4]dioxine group in probe **B** (i.e., difference in the energies of the HOMOs between probe B and probe BH = 0.04179 eV), as compared to the thiophene in probe A (i.e., difference in the energies of the HOMOs between probe A and probe AH = 0.04390 eV, Table 1. The increased steric bulk in probe **B** from the 1,2-dioxoethyl group may also hinder contact with NADH resulting in reduced hydride transfer, i.e., a kinetic effect. Probes A and B exhibit slower reaction times, attributed to charge delocalization through their π -extended thiophene bridge connections. In contrast, cyanine dyes lacking this thiophene bridge connection

demonstrate much quicker response times, typically within 6 minutes.35 Probe C initially exhibited an absorption peak at 441 nm in the absence of NADH, with no detectable fluorescence under these conditions (Fig. S16, ESI†). Upon the introduction of NADH into the probe's buffer solution, a new absorption peak emerged at 650 nm (Fig. S16, ESI†). Additionally, the probe demonstrated a notable fluorescence turn-on effect at 575 nm when excited at 420 nm. This turn-on effect featured a distinct blue shift that intensified as the concentration of NADH increased (Fig. S16, ESI†). However, when excited at 680 nm, probe C showed minimal near-infrared fluorescence (Fig. S17, ESI†). Conversely, probe D showed no fluorescence and displayed only an absorption peak at 334 nm in the absence of NADH. Nevertheless, with the gradual addition of NADH, a new absorption peak at 478 nm became apparent, accompanied by subsequent turn-on fluorescence at 625 nm (Fig. S18, ESI†). Probe E also exhibited non-fluorescence initially, with an absorption peak at 581 nm in the absence of NADH. However, as the concentration of NADH gradually increased, it revealed a broad absorption peak at 800 nm and exhibited turn-on fluorescence at 661 nm under excitation at 580 nm (Fig. S19, ESI†). Notably, probes C to E exclusively demonstrated turn-on fluorescence in visible regions, unlike probes A and B, which displayed both absorption and emission in the near-infrared region. This

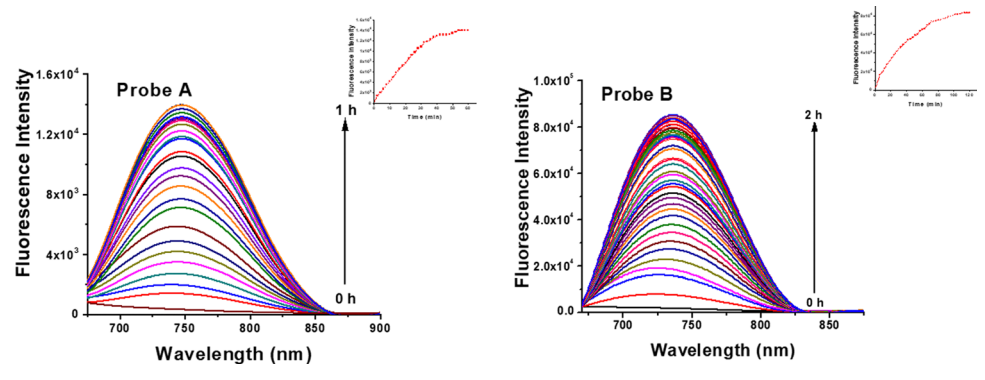


Fig. 3 Time-dependent emission profiles of 10 μM probes A and B upon exposure to 50 μM NADH, conducted in pH 7.4 phosphate buffer containing 10% DMSO under excitation at 630 nm.

	EXPT (nm)	APFD (nm)	CAM-B3LYP (nm)	Δ (APFD-EXPT) eV	D(CAM- B3LYP-EXPT) eV	APFD E(TD-HF/TD-DFT) $(H)^a$	CAM-B3LYP E (TD-HF/TD-DFT) $(H)^a$	E(APFD)-E (CAM-B3LYP) (H)
A(cis)	438	467	412	0.18	0.18	-1984.818893	-1985.311571	0.492678
AH(cis)	647	595	564	0.17	0.28	-1985.601542	-1986.097706	0.496164
A (trans)	438	478	438	0.24	0.00	-1831.271992	-1831.732996	0.461004
AH(trans)	647	587	564	0.20	0.28	-1832.055167	-1832.51637	0.461203
В	470	493	450	0.12	0.12	-2059.016602	-2059.563708	0.547106
BH	683	585	561	0.30	0.39	-2059.794338	-2060.342554	0.548216
C(cis)	441	494	443	0.30	0.01	-1984.86031	-1985.354739	0.494429
CH(cis)	650	651	596	0.00	0.17	-1985.645877	-1986.139674	0.493797
D	478	494	431	0.08	0.28	-1714.35789	-1714.815411	0.457521
DH	625	631	560	0.02	0.23	-1715.129533	-1715.593458	0.463925
E	581	495	453	0.37	0.60	-1693.499319	-1693.969182	0.469863
EH	800	619	600	0.45	0.52	-1694.283185	-1694.753073	0.469888

Table 1 Listing of calculated absorptions through TD-DFT calculations with atoms defined by 6-311+G(d) basis sets

observation underscores the pivotal role of optimizing electronwithdrawing acceptors in precisely tuning the emission of the probes to the near-infrared region (Fig. 1-3 and Fig. S16-S19, ESI†).

Theoretical calculations

Suitable models and conditions for the theoretical calculations were derived and conducted as reported previously.35 Calculated absorptions are listed in Table 1 with representations of the molecules in Fig. 4 and Fig. S28 (ESI†). An examination of probe A suggested that the two S atoms could be disposed cis or trans over the ethylenic bridge connecting the 3-methyl- $3\lambda^4$ -benzo[d]thiazole and thiophene groups and it was decided to optimize both these geometries for probes A and B and their hydride derivatives probes AH and BH, respectively. Surprisingly there is not much difference in the

calculated absorptions between the cis- and trans-geometries for probe A(cis) 467 to A(trans) 478 nm and probe AH(trans) 587 to AH(cis) 595 nm, Table 1, and Fig. 4. However, the total electronic energies for the cis conformations are slightly lower, Table 1, e.g., A(cis) at -1984.818893 H compared to A(trans) at -1831.271992 H. For that reason, when required the cis geometries were calculated. With few exceptions, most notably for probes E (0.37 and 0.60 eV for Δ (APFD-EXPT)³⁶ and Δ ((CAM-B3LYP)-EXPT) respectively) and EH (0.45 and 0.52 likewise), the calculated values for the probes are within or close to the expected range (i.e., 0.20-0.25 eV)³⁷ to those obtained experimentally, Table 1. It is also interesting that the CAM-B3LYP functional resulted in lower total electronic energies on the order of 0.45 to 0.55 H.

We calculated the absorptions using the CAM-B3LYP³⁹ functional since a theoretical study of over 100 organic dye

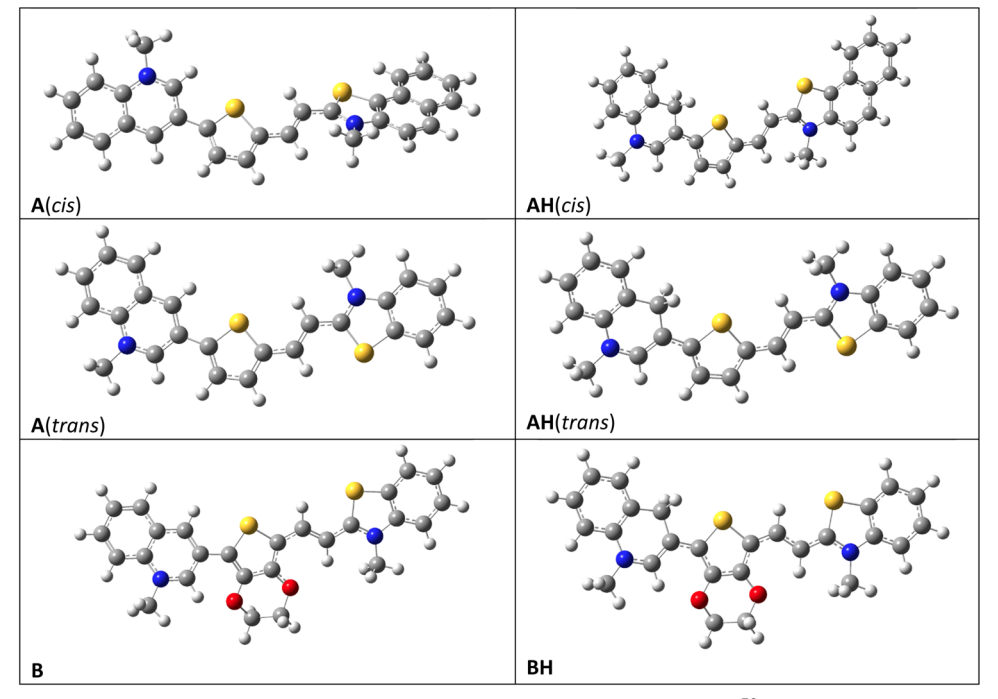


Fig. 4 Drawings of the molecules A and AH (cis and trans), B, and BH listed in Table 1 using GausView.³⁸ Drawings of C, D, E, CH, DH, and EH are in the ESI,† Fig. S28.

^a Total electronic energy.

compounds had concluded that this functional was "wellsuited for studying dyes with a very delocalized excited state". 40 The data in Table 1 from the calculations show a slightly closer set of values to the experimental for those obtained with the APFD⁴¹ functional (overall Δ 54 nm) compared to those obtained with the CAM-B3LYP functional (overall Δ 69 nm).

Planar geometries were obtained for all optimized geometries for the probes with hydride addition, i.e., AH-EH. In probe A(cis), none of the three rings were coplanar with interplanar angles of 30.81° and -32.16° between the central thiophene group and the 1-methyl-1-quinoline and the 3-methyl-3benzo[d]thiazole groups. For probes B-E, interplanar angles of 22.25°, 30.34°, 30.83°, and 27.74°, were obtained between the central thiophene group and the 1-methyl-1-quinoline with the different groups on the right of the molecules illustrated in Fig. 4 and Fig. S28 (ESI†) coplanar with the central group. The addition of a hydride atom in probes AH-EH forces a coplanar arrangement with the methylene hydrogen atoms on the 1methyl-1,4-dihydroquinoline situated equidistant from the nearby S atom on the central thiophene resulting in less steric hindrance in the molecules.

Current density diagrams, Fig. 5, were plotted to illustrate the electronic transitions and to determine the effects of the hydride addition to the probes. The colors in Fig. 5 indicate that in the case of A(cis) and B, the transitions originate from the central "thiophene" moiety and shift onto the electron-deficient 1methyl-1-quinoline groups situated on the left side of the molecules. In contrast with probes C-E, the transitions appear to end up with electron density on the right side of the molecule.

Note that these molecules, i.e., probes A-E, did not converge to an overall planar geometry in contrast to those on the right side of Fig. 5. The illustrations for probes AH(cis), BH, CH, DH, and EH show that the addition of the hydride changes the nature of the transition which in these cases originate from the electron-rich 1-methyl-1,4-dihydroquinoline groups and transition to the right side through the central "thiophene" groups and ends up on the 3-methyl-3-benzo[d]thiazole groups. The fact that the geometries of these molecules are planar presumably facilitates more delocalized transitions which are now obtained at longer wavelengths as illustrated in Table 1.

Probe selectivity and biocompatibility

Probes A and B demonstrate remarkable selectivity towards 50 µM NAD(P)H when compared across a broad spectrum of other substances. This includes 100 µM cations such as Na⁺, K⁺, Co²⁺, Fe³⁺, and Ca²⁺; 100 μM anions like Cl⁻, NO₃⁻, NO₂⁻, HCO₃⁻ and SO₄²⁻; and 100 µM biothiols such as cysteine and glutathione. Furthermore, the selectivity encompasses amino acids such as lysine, glycine, and methionine, as well as carbohydrates like galactose, ribose, glucose, fructose, pyruvate, and lactate, as depicted in Fig. S20 and S21 (ESI†). The unique ability of probes A and B to specifically focus on NAD(P)H with little or no interference from other compounds allows for accurate determination of this significant molecule within biological samples. The photostability of fluorescent probes plays a crucial role in various scientific and

biomedical applications. Within this investigation, we evaluated the probe photostability via their exposure to sustained excitation at 630 nm over a span of two hours (Fig. S22 and S23, ESI†). Both probes exhibited exceptional photostability, with fluorescence intensity decreasing by less than 3% over the entire experimental period. These findings underscore the suitability of probes A and B for prolonged imaging applications and highlight their potential as reliable tools in fluorescence imaging applications.

Based on the MTT assay results showing over 80% cell viability at concentrations up to 50 µM, probes A and B demonstrate excellent biocompatibility and low cytotoxicity for bioimaging applications (Fig. S25, ESI†). The high cell viability indicates the probes are well-tolerated by cells and do not induce significant cytotoxic effects even at relatively high concentrations (Fig. S25, ESI†). The minimal impact on cell health and metabolism is a crucial factor that makes these probes well-suited for cellular imaging studies. Effective probes must produce sufficient fluorescence signal intensity without perturbing the native cellular state. The preservation of normal physiological processes is key for accurate investigation of metabolic dynamics like NADH flux.

NAD(P) detection in live cells

Given probe A's rapid response and excellent biocompatibility, we selected it for further cellular imaging applications. A549 cells or Fibroblast cells were pretreated with 15 μM NADH in glucose-free DMEM for 30 minutes to raise intracellular NADH levels followed by incubation with 5 µM of probe A in glucosefree DMEM for varying times up to 120 minutes (Fig. 6 and Fig. S26, ESI†). Remarkably, cellular fluorescence plateaued within 30 minutes of probe A exposure and showed no additional increase with longer incubations. This indicates significantly faster activation of probe A inside living cells compared to the 60 minutes required for full turn-on in cuvette studies. This exciting finding highlights the rapid intracellular response kinetics of probe A, enabling real-time visualization of NADH fluctuations on short timescales.

Accurate measurement of intracellular NAD(P)H levels is imperative for various cellular processes, such as energy production and redox homeostasis. 5,11-25 To perform accurate assessments within live cells, the employment of compatible probes possessing sensitivity and selectivity is paramount. We further employed probe A to quantify intracellular NAD(P)H levels in live A549 cells. Subjecting the cells to a 30-minute incubation period with 5 µM of probe A yielded discernible fluorescence, signifying the presence of NAD(P)H within the cellular milieu (Fig. 7). To validate the specificity of probe A, we conducted supplementary experiments involving pre-treatment of A549 cells with diverse NADH concentrations from 5 μM, 20 μM to 50 μM for 30 minutes, followed by a subsequent 30-minute incubation with 5 μM of probe A (Fig. 7). As anticipated, we observed a progressive enhancement in cellular fluorescence signal as NADH concentrations increased, thereby affirming the robust selectivity of probe A toward NADH. This investigation underscores the efficacy and dependability of probe A as a precise tool for detecting and quantifying intracellular NAD(P)H levels in live cell environments.

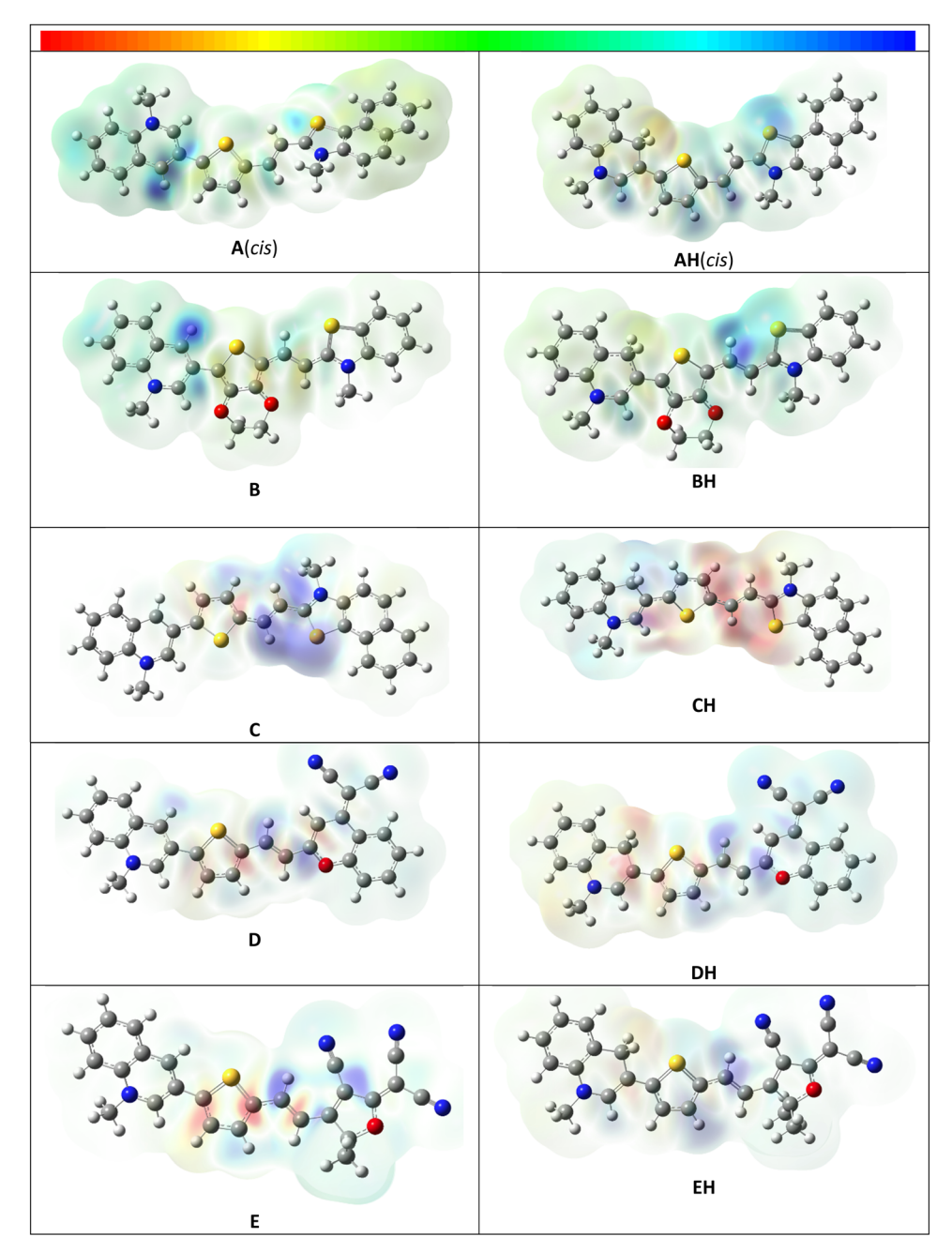


Fig. 5 Visualization of current density transitions from HOMO to LUMO for probes A(cis), AH(cis), B, and BH. Values for the scale at the top of the figure are: $A(cis) \pm 1.227 e^{-4}$, $AH(cis) \pm 5.650 e^{-5}$, $B \pm 1.121 e^{-4}$, $BH \pm 8.432 e^{-5}$, $C \pm 5.081 e^{-5}$, $CH \pm 5.317 e^{-5}$, $D \pm 5.118 e^{-5}$, $DH \pm 5.297 e^{-5}$, $E \pm 5.193 e^{-5}$, and **EH** $\pm 5.125 \text{ e}^{-5}$.

Glucose provides energy for cells via metabolic pathways like the citric acid cycle, glycolysis, and oxidative phosphorylation.⁴² In the course of glucose metabolism, NADH is generated and acts as a vital electron contributor in the electron transport chain within the citric acid cycle, culminating in ATP synthesis—the cell's fundamental energy unit. Hence, the presence of glucose and its subsequent metabolism influence cellular NADH levels. 42 Probe A is also capable of monitoring NADH levels alongside exogenous glucose. A549 cells and fibroblast cells were pretreated with varying glucose

concentrations from 0-20 mM for 30 minutes, then incubated with 5 µM probe A for an additional 30 minutes. We observed a direct correlation between increases in glucose levels and cellular fluorescence intensity (Fig. 8 and Fig. S27, ESI†). This confirms that probe A can dynamically monitor NADH fluctuations during glycolytic glucose metabolism. Intriguingly, basal NAD(P)H levels appeared higher in A549 versus fibroblast cells (Fig. 8 and Fig. S27, ESI†). Real-time monitoring of NADH concentrations during glucose metabolism is useful for the determination of cellular bioenergetics and associated

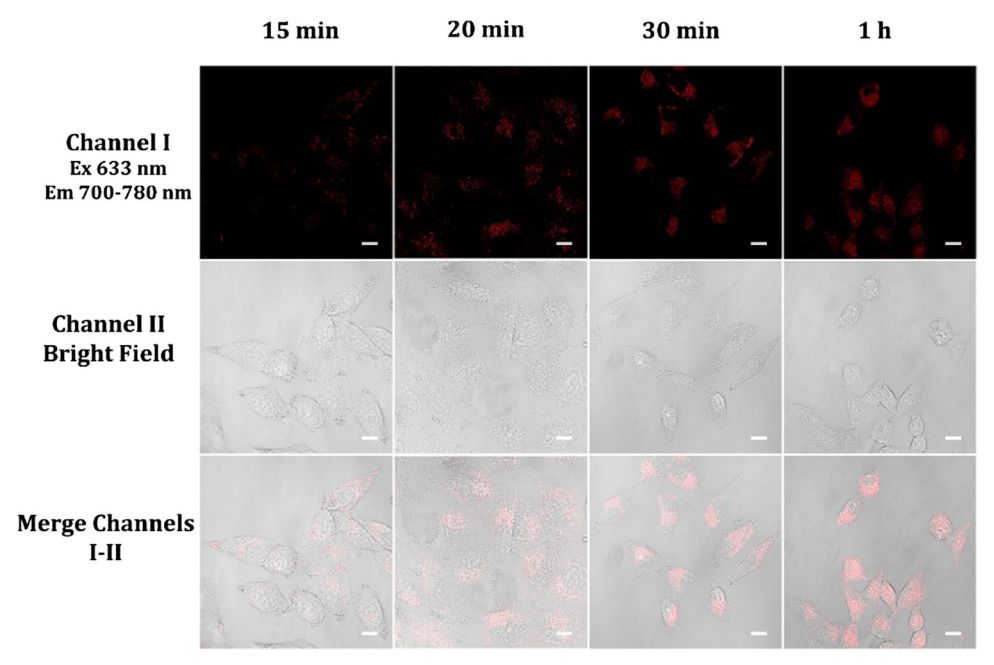


Fig. 6 Fluorescence visuals depicting A549 cells pre-exposed to 15 μM NADH within glucose-depleted DMEM medium for a 30-minute span with subsequent addition of 5 μ M of probe **A** in glucose-depleted DMEM medium across varying incubation periods. Fluorescence emissions, encompassing the range from 700 nm to 780 nm, were captured under 633 nm excitation (scale bar 50 μ m).

disorders. Aberrant glucose utilization and NADH concentrations have been implicated in diseases like cancer, diabetes, and neurodegeneration. Overall, probe A has the potential to offer unprecedented insights into the effects of glucose on NADH concentration thereby illuminating one aspect of redox biology.

NADH is also produced during the Krebs cycle in mitochondria, and its utilization by the electron transport chain generates ATP through oxidative phosphorylation. 3-6 To specifically target mitochondria, probes with a high affinity for the negatively charged mitochondrial membrane can be utilized. We theorized that probe A, possessing a dual positive charge,

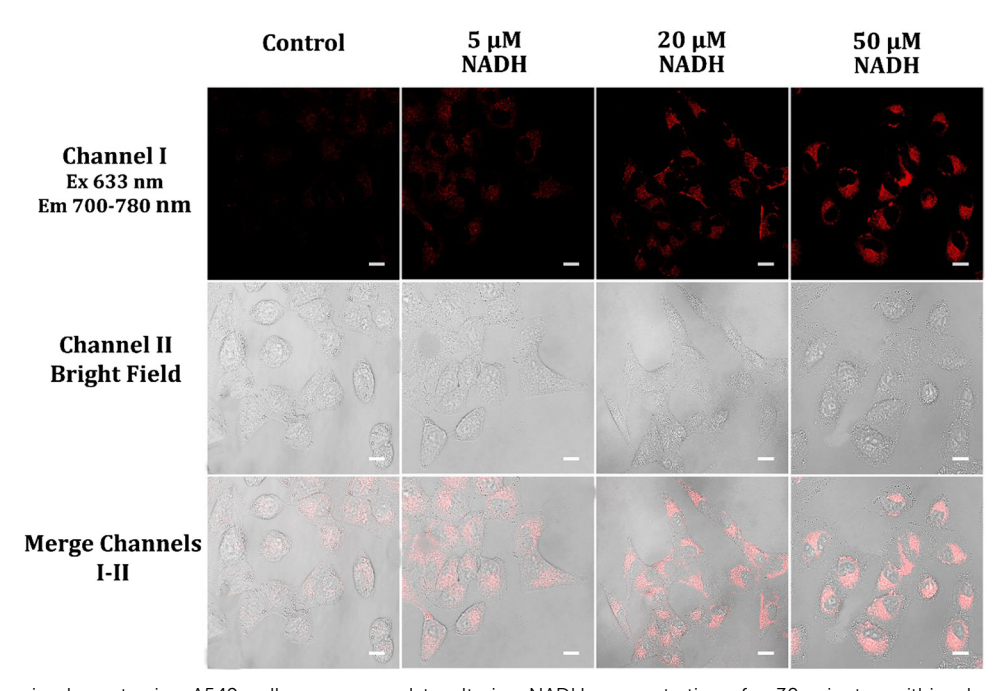


Fig. 7 Fluorescence visuals portraying A549 cells pre-exposed to altering NADH concentrations for 30 minutes within glucose-depleted DMEM medium, succeeded by a 30-minute incubation with 5 µM of probe A in glucose-depleted DMEM medium. Fluorescence emissions were captured in the range of 700 nm to 780 nm under 633 nm excitation for both sets of visuals (scale bar 50 μ m).

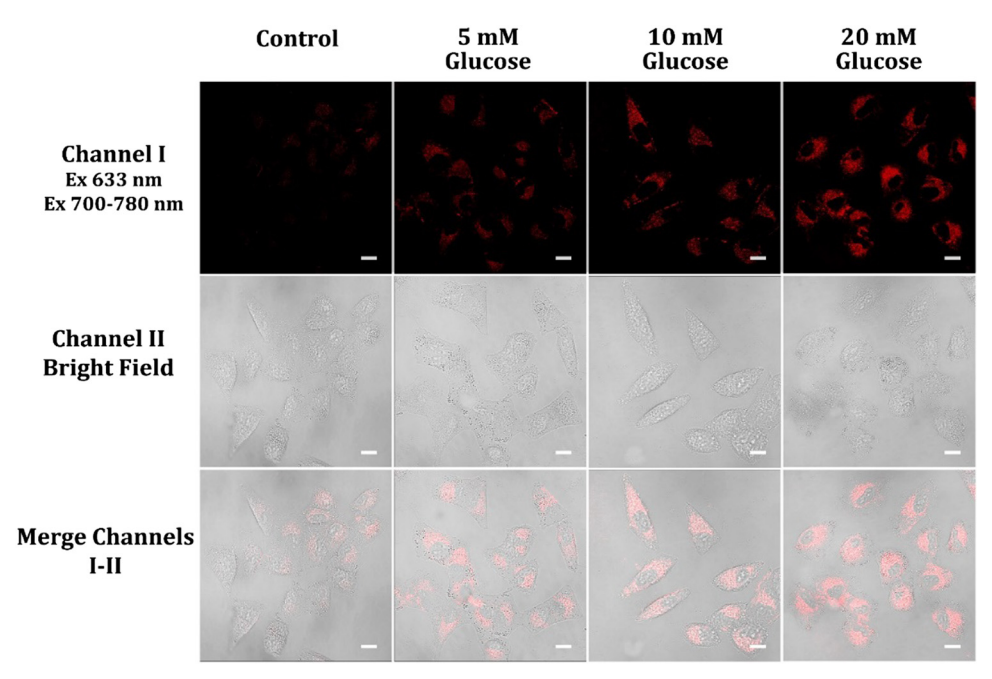


Fig. 8 Fluorescence visuals displaying A549 cells pre-exposed to different glucose concentrations ranging from 0, 5, 10 to 20 mM within glucosedepleted DMEM medium for 30 minutes, followed by an additional 30-minute incubation with 5 μM of probe A in glucose-depleted DMEM medium. Additionally, a control visual of A549 cells incubated with 5 μM probe A in glucose-depleted DMEM medium for 30 minutes is included. Fluorescence images were collected in the range of 700 nm to 780 nm under 633 nm excitation with scale bars of 50 μm.

might specifically engage with mitochondria via electrostatic connections. A co-incubation study was conducted, wherein probe A was combined with MitoView 405—a readily available dye recognized for its mitochondrial targeting in A549 cells. A high Pearson correlation coefficient of 0.96 linking probe A with MitoView 405 validated the precise mitochondrial targeting of probe A. This targeting mechanism involves the probe traversing the plasma membrane and amassing within the negatively charged mitochondria. Here, its positive charges engage with the mitochondria's negative potential, resulting in the selective homing of the probe (Fig. 9).

Multicolor imaging plays a vital role in cell biology and bioimaging, enabling the comprehensive examination of diverse cellular processes. 43 By employing distinct fluorophores to label various cellular structures and molecules, researchers can delve into the localization, dynamics, and interactions within the cell. 43 The integration of near-infrared (NIR) probes introduces an additional color channel, thus expanding the scope of components that can be visualized and enhancing the depth of information attainable.43 While visible fluorescent probes emit light within the visible electromagnetic spectrum, their simultaneous use can often lead to spectral overlap issues. In contrast, NIR probes emit light in the NIR range, facilitating a superior separation of fluorescent signals from different probes. This not only mitigates crosstalk but also guarantees more accurate and easily interpretable imaging results. To illustrate the advantages of multi-color imaging, we harnessed the potential of distinct probes: nuclei-targeting Hoechst, emitting in blue; lysosome-specific Lyso-sensor green, with a green emission; and the mitochondria-selective probe A. By co-staining with these probes, we successfully labeled different organelles with discrete fluorescence channels, all without any detrimental

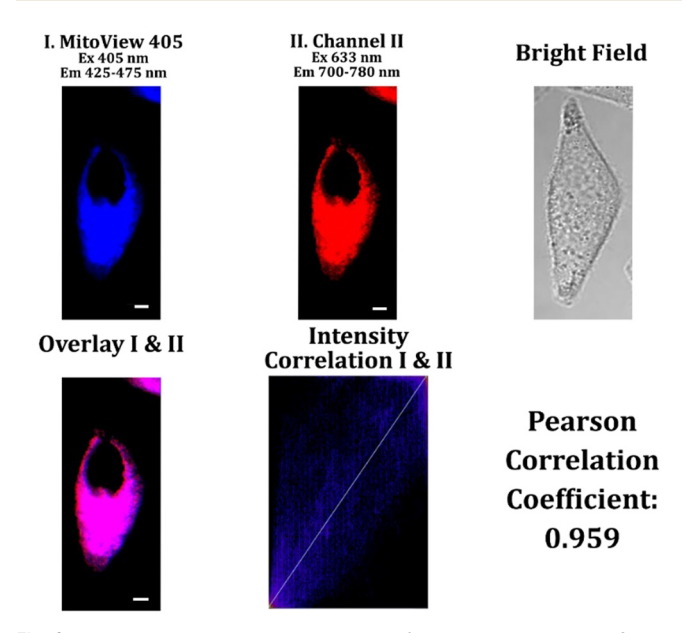


Fig. 9 Fluorescence visuals depicting A549 cells pre-exposed to 25 mM glucose within glucose-depleted DMEM medium for 30 minutes, followed by co-incubation involving 5 μ M of probe **A** and 5 μ M of the mitochondriaspecific MitoView 405 within glucose-depleted DMEM medium for an extra 30 minutes. Fluorescence visuals were captured by exciting probe A at 633 nm, with emission detected in the range of 700 nm to 780 nm. Simultaneously, MitoView 405 was excited at 405 nm, with emission captured within 425 nm to 475 nm with a scale bar of 20 μm.

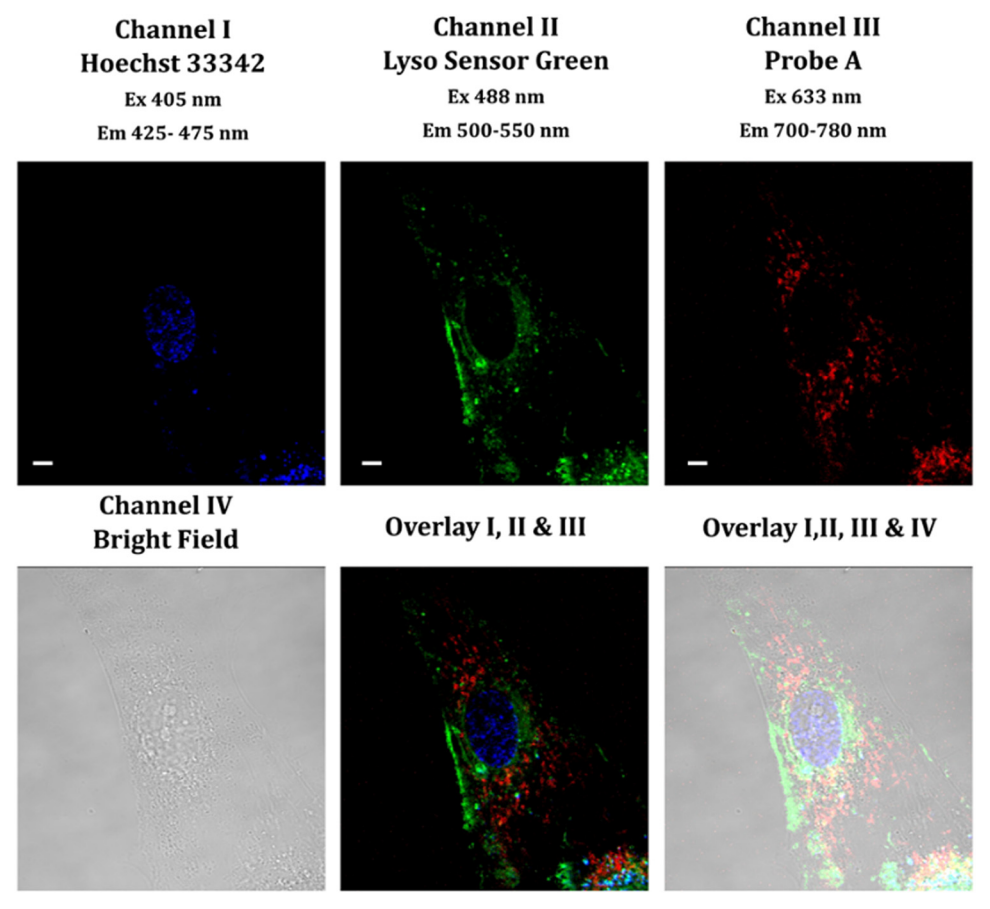


Fig. 10 Cellular fluorescence images of fibroblast cells after an initial 30-minute pre-treatment with 10 mM glucose in cell medium, followed by coincubation with 5 μ M of the nucleus-specific stain Hoechst 33342, 5 μ M of the lysosome-specific marker LysoSensor Green, and 5 μ M of probe **A** in cell medium for an additional 30 minutes. Fluorescence imaging was performed in specific wavelength ranges: Hoechst 33342 images were acquired between 425 nm and 475 nm under excitation at 405 nm, LysoSensor Green images were captured between 500 nm and 550 nm under excitation at 488 nm, and probe A images were recorded in the range of 700 nm to 780 nm under excitation at 633 nm with scale bars of 20 µm.

crosstalk (Fig. 10, and Fig. S28, S29, ESI†). This was unequivocally validated by the remarkably low Pearson Correlation coefficients associated with the distinct fluorescence signals (Fig. S28 and S29, ESI†).

Vital metabolites, such as lactate and pyruvate, are also significant for cellular energy metabolism^{44,45} as they regulate NAD(P)H levels. Lactate is produced as a byproduct of anaerobic metabolism, and it can be converted back into pyruvate in a process called the Cori cycle. 46-48 Furthermore, cells can actively uptake lactate, channeling it into mitochondria for oxidation, subsequently generating ATP. 49 This mechanism is recognized as the 'lactate shuttle', gaining particular significance in tissues characterized by elevated energy requirements, like cardiac tissue skeletal and muscle. 46,50 Pyruvate serves as a pivotal intermediary in both glycolysis and the TCA cycle, capable of transformation into acetyl-CoA for subsequent involvement in oxidative phosphorylation.⁵¹ Our study unveiled that subjecting probe A treated A549 cells to 10 mM lactate resulted in an elevation of cellular fluorescence intensity, signifying a concurrent rise in NAD(P)H levels (Fig. 11). In contrast, treating the cells with 5 mM pyruvate led to a decrease in cellular fluorescence intensity, indicating a decrease in NAD(P)H levels (Fig. 11). The cellular fluorescence signal was notably higher in cells treated with a blend of 5 mM pyruvate and 10 mM lactate, in comparison to untreated control cells (Fig. 11). These findings imply an intricate modulation of NAD(P)H levels within live cells upon the concurrent influence of lactate and pyruvate.

Solid tumors often exhibit low oxygen levels or hypoxia, a prevalent characteristic that can substantially impact cellular metabolism. 52-54 Under hypoxic conditions, cells rely on anaerobic glycolysis to produce energy, leading to an accumulation of lactate and reduced oxidative phosphorylation. 52-54 This transition in metabolism can exert an influence over NAD(P)H levels within live cells. NADH generation transpires during glycolysis, whereas NAD(P)H assumes a pivotal role in upholding redox equilibrium and biosynthesis pathways. 52-54 CoCl₂ has been established to simulate hypoxia-like conditions within cancer cells by enhancing the stability of the transcription factor HIF-1α. This factor is notably overexpressed in numerous cancer cells and governs genes implicated in metabolism, angiogenesis, and cellular survival.^{55–57} We examined the impact of CoCl₂ pre-treatment on the fluorescence intensity of A549 cells upon probe A exposure. The findings unveiled a proportional enhancement in cellular fluorescence intensity as A549 cells underwent pre-treatment with

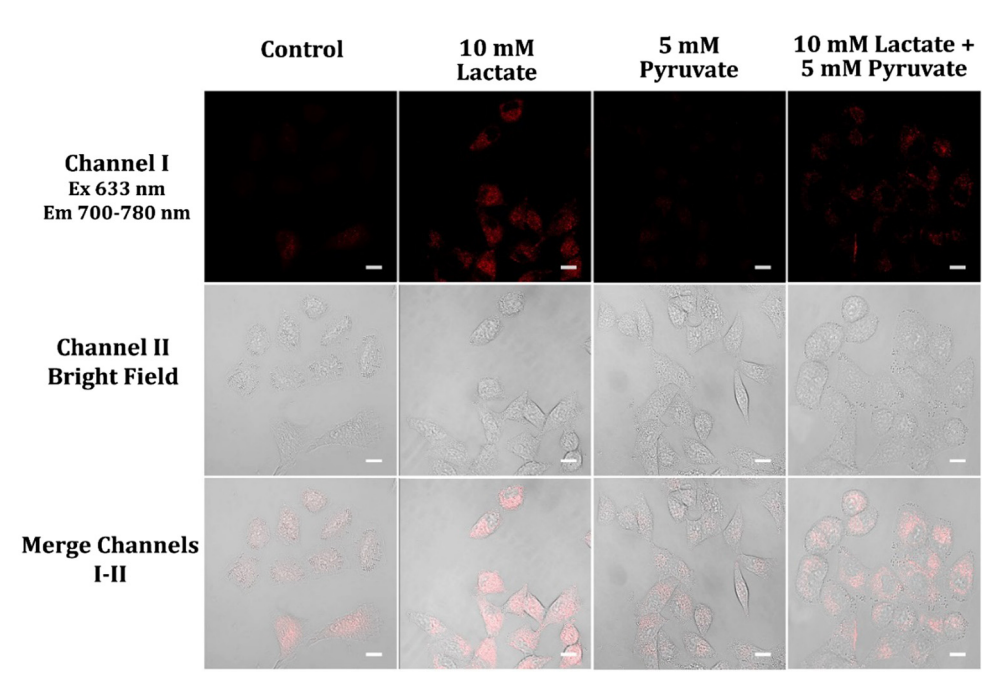


Fig. 11 Fluorescence visuals displaying diverse A549 cell conditions, including pre-treatment with lactate, pyruvate, or a dual combination of both within glucose-depleted DMEM medium, over a 30-minute span. Subsequently to this, the cells were subjected to an additional 30-minute incubation with 5 μM of probe A within glucose-depleted DMEM medium. Fluorescence visuals were captured under 633 nm excitation, with emission captured within the 700 nm to 780 nm range with scale bars of 50 μ m.

ascending CoCl2 concentrations from 50, 100, to 150 µM. This enhancement signified an elevation in NAD(P)H levels (Fig. 12). This suggests that CoCl₂ treatment can alter cellular metabolism and increase levels of NAD(P)H within cancer cells by inducing a hypoxic-like state. This culminates in heightened lactate production and augmented NAD(P)H levels. The employment of fluorescent probes such as probe A can aid in visualizing fluctuations in NAD(P)H levels due to CoCl2 exposure.

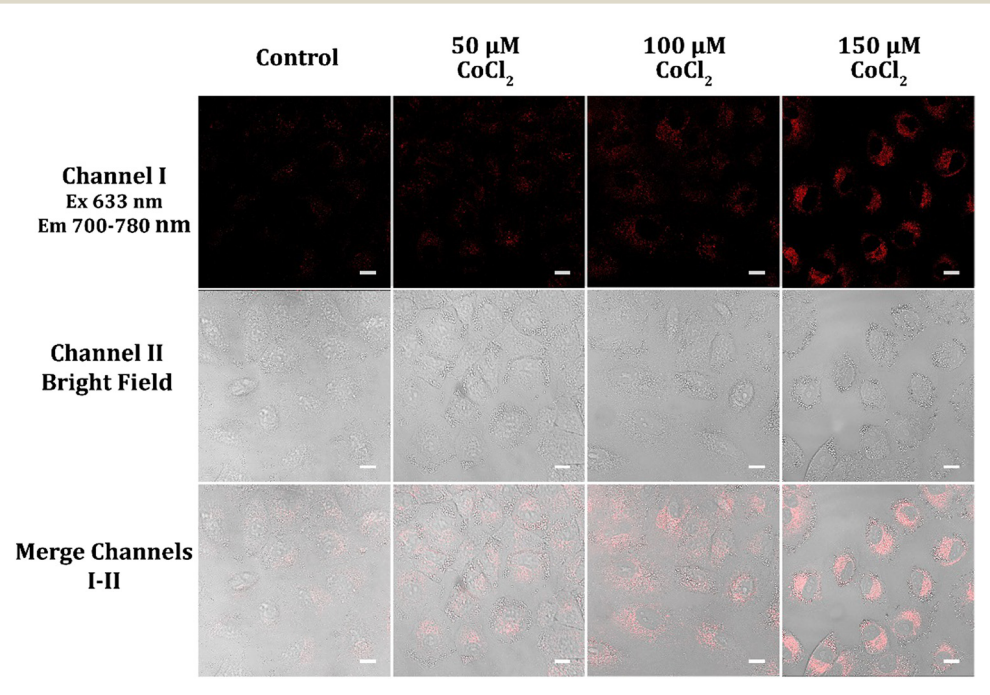


Fig. 12 Fluorescence visuals depicting A549 cells subjected to pre-treatment with diverse $CoCl_2$ concentrations from 50, 100 to 150 μ M within glucosefree DMEM medium for a 12 h duration. Afterwards, the cells were subjected to an additional 30-minute incubation with 5 μ M of probe **A** within glucosefree DMEM medium. Fluorescence images were captured under 633 nm excitation, with emission recorded within the 700 nm to 780 nm range with scale bars of 50 µm.

Gemcitabine, a widely used chemotherapy drug, is highly effective in treating an array of cancer types, such as pancreatic, bladder, and lung cancer. 58-63 Its mechanism of action involves impeding cancer cell replication and disrupting DNA synthesis, ultimately resulting in programmed cell death apoptosis. 58-63 Categorized as a nucleoside analog, gemcitabine incorporates into DNA, causing chain termination and preventing cancer cells from dividing. 58-63 Our research findings confirm that treatment of A549 cancer cells with gemcitabine at varying doses leads to enhanced levels of coenzymes NAD(P)H (Fig. 13). These shifts in cellular metabolic processes and energy production could potentially augment the anticancer impacts of gemcitabine, creating conditions of cellular stress and perturbing energy dynamics within cancer cells.⁵⁸⁻⁶³ In summary, gemcitabine, a potent chemotherapy agent, possesses the capability to influence cancer cell metabolism and energy processes through multifaceted mechanisms.⁵⁸⁻⁶³ These changes may contribute to the drug's anticancer efficacy by inducing cellular stress and triggering programmed cell death or apoptosis. Deeper investigations are warranted to achieve a comprehensive understanding of how gemcitabine modulates NAD(P)H levels and cellular metabolism within cancer cells, with the aim of refining therapeutic strategies.

Camptothecin is a chemotherapeutic agent that potently inhibits the enzyme DNA topoisomerase I, which plays a vital role in DNA synthesis and transcription. By disrupting topoisomerase I activity, camptothecin interferes with DNA replication and causes double strand breaks that trigger apoptosis in cancer cells. As an inhibitor of this essential nuclear enzyme, camptothecin exhibits cytotoxic effects that have shown antineoplastic potential against various types of cancer. 64-69 This

inhibition leads to the accumulation of DNA strand breaks and triggers the activation of PARP enzymes.⁶⁴⁻⁶⁹ Consequently, a depletion of NAD⁺ levels occur, while NADH levels increase, exerting an impact on cellular metabolism and energy creation. 64-69 Moreover, camptothecin treatment has an impact on NAD(P)H levels in cancer cells. NAD(P)H, primarily synthesized via the pentose phosphate pathway (PPP), assumes a crucial role in upholding cellular redox equilibrium and supporting diverse biosynthetic processes. The DNA damage induced by camptothecin activates DNA repair mechanisms and triggers oxidative stress responses, 70-72 leading to an increased demand for NAD(P)H. Consequently, the PPP is upregulated to meet the necessary supply of NAD(P)H required for antioxidant defense mechanisms, including the regeneration of reduced glutathione (GSH) and thioredoxin, as well as biosynthesis. 73-75 Thus, camptothecin treatment ultimately results in elevated NADH and NAD(P)H levels in cancer cells. In our study, we conducted assays using varying doses of camptothecin, observing a subsequent rise in NADH and NAD(P)H levels within A549 cancer cells, as depicted in Fig. 14. The increase of NADH concentration in the cancer cells may be attributed to enhanced glycolysis and oxidative stress, while the elevation in NAD(P)H levels arises from the activation of the pentose phosphate pathway, fulfilling the heightened demand for cellular redox balance and biosynthetic processes, Fig. 14.⁷³⁻⁷⁵

Cisplatin, a widely utilized chemotherapy drug for various cancers, including lung cancer, exerts its therapeutic effects by chelating to DNA molecules preventing replication and ultimately resulting in cell death. 76-81 Recent studies have revealed that cisplatin can also influence NAD(P)H concentrations

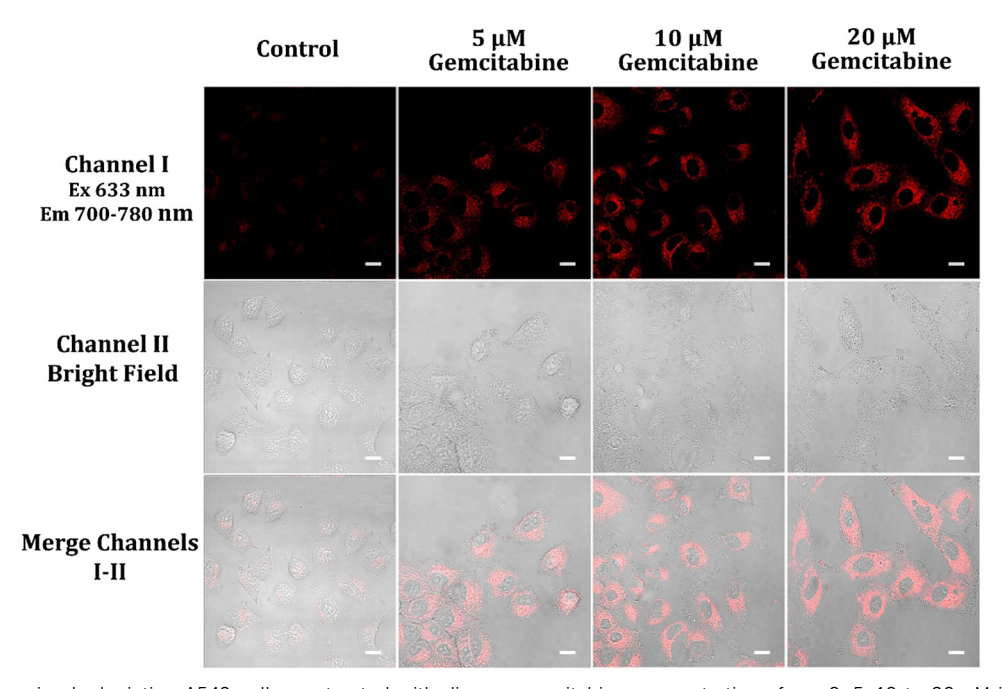


Fig. 13 Fluorescence visuals depicting A549 cells pre-treated with diverse gemcitabine concentrations from 0, 5, 10 to 20 μM in glucose-depleted DMEM medium for 2 hours, followed by a 30 minute incubation with 5 µM of probe A in glucose-depleted DMEM medium. Fluorescence was excited at 633 nm, and emissions were captured between 700 nm and 780 nm with scale bars of $50~\mu m$.

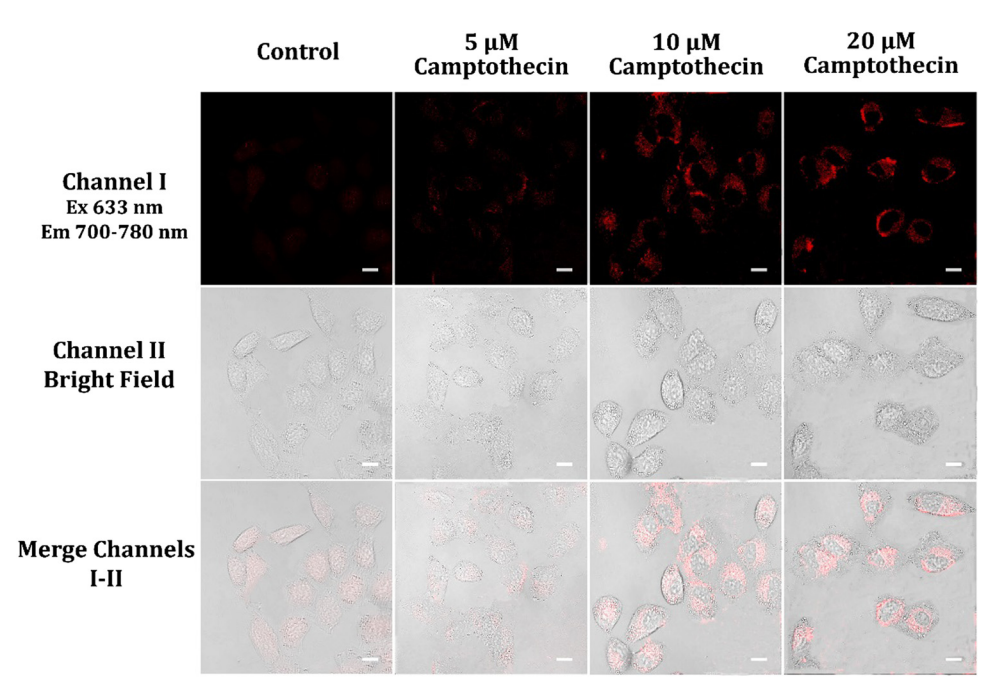


Fig. 14 Fluorescence visuals illustrating A549 cells subjected to pre-treatment with varying concentrations of camptothecin from 0, 5, 10 to 20 μM in glucose-depleted DMEM medium for 2 hours, followed by a 30-minute incubation with 5 μ M of probe **A** in glucose-depleted DMEM medium. Fluorescence visuals were acquired using 633 nm excitation, with emissions detected between 700 nm and 780 nm with scale bars of 50 µm.

within malignant cells. We treated cells with different doses of cisplatin for 2 hours in a medium devoid of glucose, followed by a subsequent 30-minute incubation with a fluorescent probe in the same medium, Fig. 14. We find that treatment with varying doses of cisplatin (0, 5, 10, and 20 µM) results in elevated NAD(P)H levels inside A549 cells, as indicated by the

intensified fluorescence intensity observed in the images (Fig. 15). This suggests that cisplatin has interfered with cellular metabolic processes and energy generation in cells, perhaps contributing to its anticancer properties. The exact mechanism by which cisplatin enhances NAD(P)H levels remains unclear; however, it may involve alterations in cellular

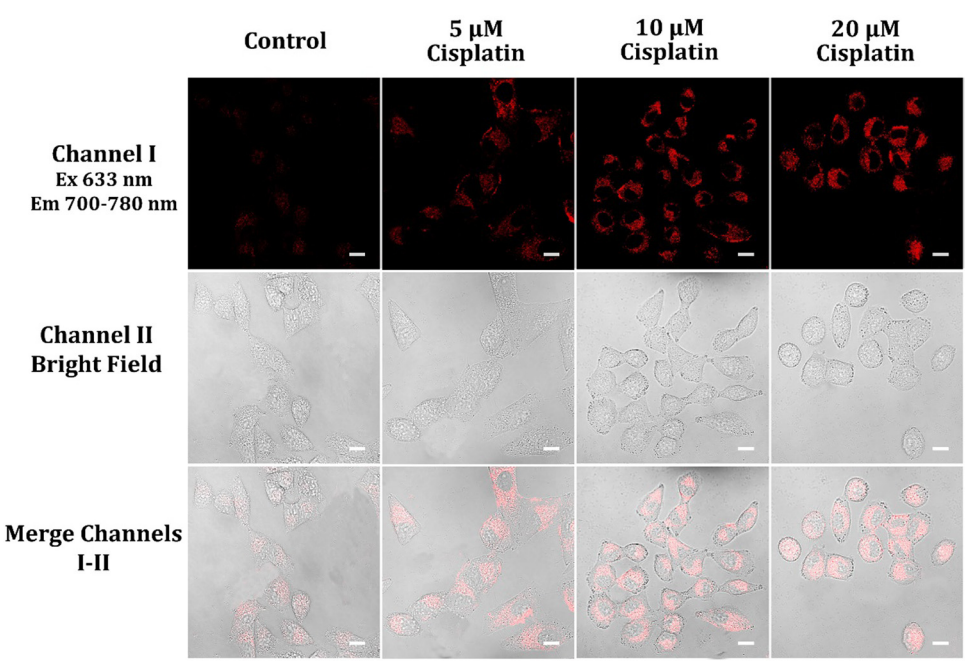


Fig. 15 Fluorescence visuals of A549 cells subjected to pre-treatment with varying cisplatin concentrations from 0, 5, 10 to 20 μM for 2 hours within a glucose-depleted DMEM medium. Subsequently, the cells were exposed to 5 µM of probe A for 30 minutes under the same medium. The captured fluorescence images encompass the range of 700 nm to 780 nm, with excitation occurring at 633 nm with scale bars of 50 µm.

redox balance and energy metabolism. It is possible that hindering the replication of DNA, a process which should consume energy, results in this increase. Alternatively, cisplatin may influence the activity of enzymes involved in NAD(P)H biosynthesis and regeneration. Nonetheless, additional research is needed to elucidate the intricate mechanisms at play and delve into cisplatin's therapeutic implications in cancer therapy.

NAD(P)H Detection in the Early Larval Stage of D. melanogaster

Detecting NADH and NAD(P)H levels in the early larval stage of D. melanogaster may afford insights into various metabolic processes, including energy production, redox reactions, biosynthesis, and cellular defense against oxidative stress.82 To ensure reproducibility, newly starved larvae of D. melanogaster are utilized due to their consistent and low levels of NAD(P)H. By selecting larvae from the same developmental stage and subjecting them to a standardized starvation protocol, a consistent baseline NAD(P)H level can be established among the experimental subjects. This controlled approach minimizes potential confounding factors resulting from variations in NAD(P)H levels due to different developmental stages or feeding conditions. As a result, the reproducibility of the experimental results and more accurate comparison of NAD(P)H levels between different treatments or conditions is assured.

To establish a baseline reference, a control experiment was conducted using freshly starvation-hatched fruit fly larvae without NADH treatment. In this control group, weak fluorescence was observed, indicating a naturally low concentration of endogenous NADH within the larvae, Fig. 16. This control experiment serves as a crucial comparison point, highlighting

the minimal fluorescence signal attributed to the inherent NADH levels in the larvae. The contrast between the weak fluorescence in the control group and the increased fluorescence intensity observed with NADH treatment provides further evidence that the observed fluorescence changes are specifically caused by the presence of exogenously administered NADH. The absence of significant fluorescence in the control group also confirms that the measured fluorescence signal is not influenced by background noise or unrelated factors, reinforcing the specific association with NADH concentration. These results indicate that freshly starvation-hatched fruit fly larvae possess a naturally low concentration of endogenous NADH, which is substantially elevated upon treatment with exogenous NADH. This control experiment enhances our understanding of the baseline NADH levels in the larvae and establishes a foundation for comparing the fluorescence changes induced by NADH treatment.

In the experimental group, the larvae underwent treatment with various concentrations of NADH from 0, 5, 20 to 50 μM for 1 h, followed by a two-hour incubation with 10 μM of probe A, resulting in noticeable changes in fluorescence intensity, Fig. 16. The observed increase in fluorescence intensity with higher doses of NADH suggests a dose-dependent stimulatory effect of NADH on the fluorescence signal detected by probe A. This indicates the effective reduction of the probe by NADH, leading to a measurable increase in fluorescence. The dosedependent nature of the fluorescence response further supports the specificity of the observed changes to NADH concentration as higher NADH concentrations produced a more pronounced increase in fluorescence intensity compared to lower concentrations.

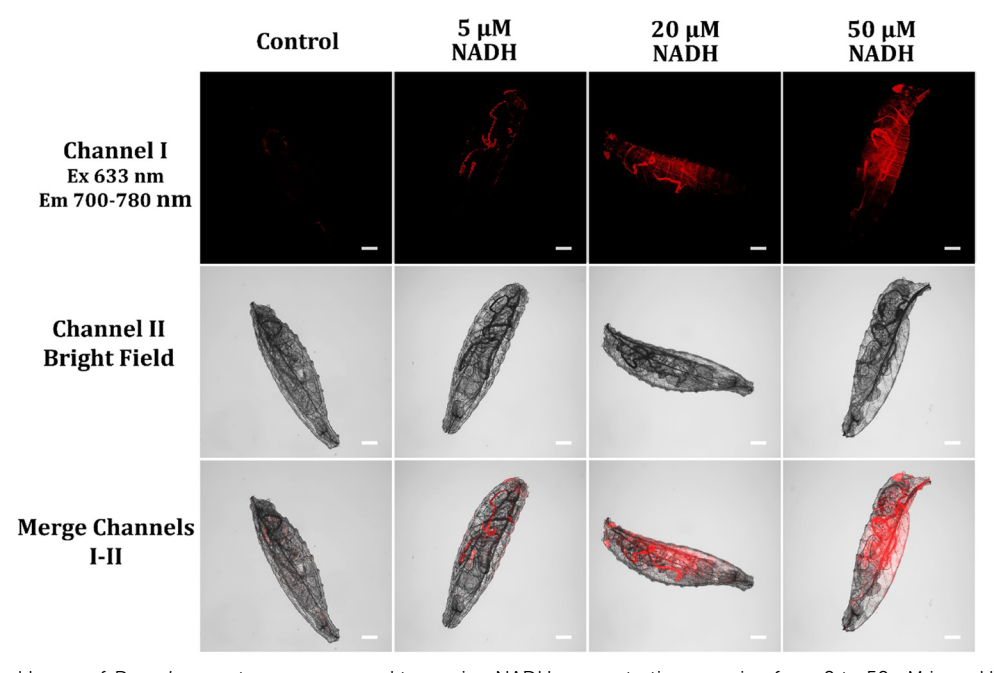


Fig. 16 Newly starved larvae of D. melanogaster were exposed to varying NADH concentrations ranging from 0 to 50 µM in a pH 7.4 PBS solution for 1 hour. Subsequently, the larvae were washed three times with the PBS solution and incubated in a PBS solution containing 10 µM of probe A for 2 hours. Fluorescence signals were captured within the 700-780 nm wavelength range under 633 nm excitation with scale bars of 200 µm.

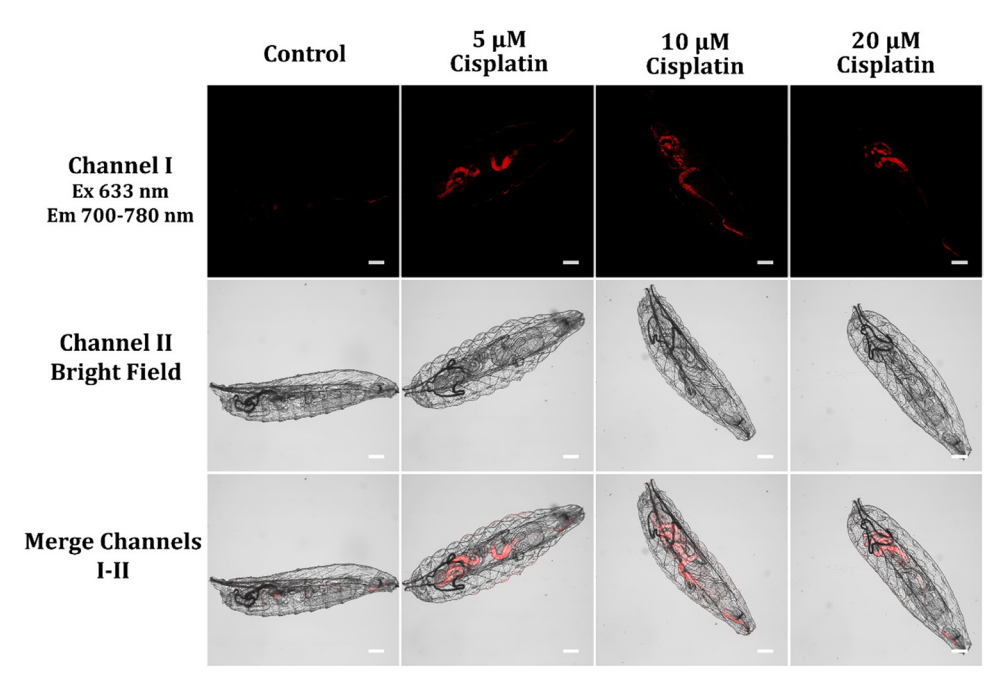


Fig. 17 Newly starved larvae of *D. melanogaster* were exposed to varying cisplatin concentrations (0 to 20 μM) in a pH 7.4 PBS solution for 2 hours. Following this, the larvae were washed thrice with the PBS solution and incubated in a PBS solution containing 10 µM of probe A for 2 hours. Fluorescence signals were captured within the 700-780 nm wavelength range under 633 nm excitation with scale bars of 200 µm.

We also examined changes in NAD(P)H levels in newly hatched fruit fly larvae subjected to different concentrations of cisplatin, employing probe A for detection (Fig. 17). The larvae underwent treatment with cisplatin in a pH 7.4 PBS solution for a duration of 2 hours, encompassing a range of concentrations from 0 to 20 µM. Subsequently, the larvae were incubated with 10 µM of probe A for an additional 2 hours in the same pH 7.4 PBS solution, followed by three washes with the PBS buffer solution. We noticed an increase in fluorescence intensity in the control larvae when exposed to cisplatin treatment in comparison to the untreated larvae (Fig. 17). This increase in fluorescence intensity indicates that cisplatin has an effect on the NAD(P)H levels within the larvae. Nonetheless, even though there was an elevation in fluorescence intensity upon cisplatin treatment, we did not note a subsequent rise in fluorescence intensity as cisplatin doses increased. This lack of a dose-dependent increase suggests the presence of a saturation point beyond which higher concentrations of cisplatin do not significantly affect fluorescence. Additional investigations are required to unveil the precise molecular pathways and mechanisms responsible for the augmentation of NAD(P)H levels subsequent to cisplatin treatment in larvae. Our results highlight the interconnectedness between cisplatin, cellular metabolism, and NAD(P)H dynamics.83,84

Conclusions

In summary, probes A and B offer near-infrared absorption and emission capabilities, ensuring minimal interference and improved tissue penetration. The probes encompass facile synthesis, adaptable optical properties, specificity to

mitochondria, glycolytic NADH monitoring, post-treatment NAD(P)H visualization, and the exploration of drug effects on cellular metabolism. Notably, probe A has proven effective in tracking NAD(P)H level changes within D. melanogaster larvae during cisplatin treatment. Their near-infrared fluorescence capacity renders them valuable tools for comprehending biological processes, aiding diagnostics, and advancing research in various settings. These fluorescent probes enable real-time NADH level detection, granting insights into drug efficacy and mechanisms for effective cancer treatments.

Materials and methods

The ESI† comprehensively details all materials and methods used in the study.

Author contributions

R. L. L. and H. Y. L. spearheaded conceptualization, methodology, project administration, supervision, manuscript writing, and funding acquisition. S. K. D. assumed the role of project leader and was responsible for the preparation of fluorescent probes. D. L. A., M. W., S. J. and J. P. contributed extensively to investigation and data analysis. Computation chemistry for the fluorescent probes was overseen by R. L. L. and D. R. T. D. L. A., M. G. and T. W. managed the fluorescence imaging of the fruit fly. B. G. collected high-resolution mass spectra of the probes, their reaction products with NADH, and contributed to manuscript enhancement.

Conflicts of interest

There are no conflicts to declare.

Acknowledgements

This research was supported by the National Institute of General Medical Sciences of the National Institutes of Health (Award Numbers R15GM114751 (granted to H. Liu), 2R15GM114751-02 (granted to H. Liu), and R15 GM146206-01 (granted to H. Liu and R. Luck)). Research was also partially supported by the National Institute of General Medical Sciences of the National Institutes of Health under award number 1R15GM152969-01 to R. L. Luck, H. Liu, and T. Werner. Financial assistance was also received from the National Science Foundation under award number 2117318, which enabled the acquisition of a new NMR spectrometer for fluorescent probe analysis (granted to H. Liu). Computational calculations on the probes were conducted using the high-performance computing infrastructure at Michigan Technological University.

References

- 1 R. N. Kujundzic, N. Zarkovic and K. G. Troselj, Crit. Rev. Eukaryotic Gene Expression, 2014, 24, 287-309.
- 2 W. H. Ying, Redox Signaling, 2008, 10, 179-206.
- 3 W. L. Xia, Z. Wang, Q. Wang, J. Han, C. P. Zhao, Y. Y. Hong, L. L. Zeng, L. Tang and W. H. Ying, Curr. Pharm. Des., 2009, **15**, 12–19.
- 4 R. P. Goodman, S. E. Calvo and V. K. Mootha, J. Biol. Chem., 2018, 293, 7508-7516.
- 5 P. J. Sun, H. X. Zhang, Y. Q. Sun and J. Liu, Spectrochim. Acta, Part A, 2021, 245, 118919.
- 6 T. S. Blacker and M. R. Duchen, Free Radical Biol. Med., 2016, 100, 53-65.
- 7 I. Mendez and M. Diaz-Munoz, Front. Endocrinol., 2018, 9,
- 8 A. A. Pramono, G. M. Rather, H. Herman, K. Lestari and J. R. Bertino, Biomolecules, 2020, 10, 358.
- 9 G. M. Rather, A. A. Pramono, Z. Szekely, J. R. Bertino and P. M. Tedeschi, Pharmacol. Ther., 2021, 226, 107864.
- 10 F. S. Omar, N. Duraisamy, K. Ramesh and S. Ramesh, Biosens. Bioelectron., 2016, 79, 763-775.
- 11 S. Y. Park, S. A. Yoon, Y. J. Cha and M. H. Lee, Coord. Chem. Rev., 2021, 428, 213613.
- 12 Y. H. Zhao, K. Y. Wei, F. P. Kong, X. N. Gao, K. H. Xu and B. Tang, Anal. Chem., 2019, 91, 1368-1374.
- 13 A. Podder, V. P. Murali, S. Deepika, A. Dhamija, S. Biswas, K. K. Maiti and S. Bhuniya, Anal. Chem., 2020, 92, 12356-12362.
- 14 A. Podder, N. Thirumalaivasan, Y. K. Chao, P. Kukutla, S. P. Wu and S. Bhuniya, Sens. Actuators, B, 2020, 324, 128637.
- 15 H. Sharma, N. K. Tan, N. Trinh, J. H. Yeo, E. J. New and F. M. Pfeffer, Chem. Commun., 2020, 56, 2240-2243.

- 16 S. N. Hong, G. T. Pawel, R. J. Pei and Y. Lu, Biomed. Mater., 2021, 16, 044108.
- 17 M. Z. Li, C. Liu, W. J. Zhang, L. F. Xu, M. M. Yang, Z. L. Chen, X. X. Wang, L. L. Pu, W. L. Liu, X. S. Zeng and T. H. Wang, J. Mater. Chem. B, 2021, 9, 9547-9552.
- 18 Y. B. Zhang, D. L. Arachchige, A. Olowolagba, R. L. Luck and H. Y. Liu, Methods, 2022, 204, 22-28.
- 19 K. Q. Ma, H. Yang, X. K. Wu, F. J. Huo, F. Q. Cheng and C. X. Yin, Angew. Chem., Int. Ed., 2023, 62, e202301518, DOI: 10.1002/anie.202301518.
- 20 Q. Wang, Y. Z. Zhu, D. B. Chen, J. L. Ou, M. Chen, Y. Feng, W. B. Wang and X. M. Meng, Talanta, 2023, 257, 124393.
- 21 J. H. Joo, D. Youn, S. Y. Park, D. S. Shin and M. H. Lee, Dyes Pigm., 2019, 170, 107561.
- 22 J. H. Joo, M. Won, S. Y. Park, K. Park, D. S. Shin, J. S. Kim and M. H. Lee, Sens. Actuators, B, 2020, 320.
- 23 Y. Tian, W. L. Jiang, W. X. Wang, G. J. Mao, Y. F. Li and C. Y. Li, Biomaterials, 2021, 271, 120736.
- 24 S. K. Dwivedi, D. L. Arachchige, A. Olowolagba, M. Mahmoud, J. Cunnien, D. R. Tucker, D. Fritz, T. Werner, R. L. Luck and H. Y. Liu, J. Mater. Chem. B, 2023, 11, 6296-6307.
- 25 M. A. Fomin, R. I. Dmitriev, J. Jenkins, D. B. Papkovsky, D. Heindl and B. Konig, ACS Sens., 2016, 1, 702-709.
- 26 G. Bonuccelli, E. M. De Francesco, R. de Boer, H. B. Tanowitz and M. P. Lisanti, Oncotarget, 2017, 8, 20667-20678.
- 27 K. Kiyose, H. Kojima and T. Nagano, Chem. Asian J., 2008, 3, 506-515.
- 28 N. Kosaka, M. Ogawa, P. L. Choyke and H. Kobayashi, Future Oncol., 2009, 5, 1501–1511.
- 29 K. Umezawa, D. Citterio and K. Suzuki, Anal. Sci., 2014, 30, 327-349.
- 30 X. D. Jiang, S. Li, J. Guan, T. Fang, X. Liu and L. J. Xiao, Curr. Org. Chem., 2016, 20, 1736-1744.
- 31 J. I. Scott, Q. Y. Deng and M. Vendrell, ACS Chem. Biol., 2021, 16, 1304-1317.
- 32 J. N. Dong, G. W. Lu, Y. Y. Tu and C. B. Fan, New J. Chem., 2022, 46, 10995-11020.
- 33 C. P. Ding and T. B. Ren, Coord. Chem. Rev., 2023, 482, 215080.
- 34 Y. L. Qi, Y. Z. Li, M. J. Tan, F. F. Yuan, N. Murthy, Y. T. Duan, H. L. Zhu and S. Y. Yang, Coord. Chem. Rev., 2023, 486, 215130.
- 35 D. L. Arachchige, S. K. Dwivedi, S. Jaeger, A. M. Olowolagba, M. Mahmoud, D. R. Tucker, D. R. Fritz, T. Werner, M. Tanasova, R. L. Luck and H. Y. Liu, ACS Appl. Bio Mater., 2023, 6, 3199-3212.
- 36 A. Austin, G. A. Petersson, M. J. Frisch, F. J. Dobek, G. Scalmani and K. Throssell, J. Chem. Theory Comput., 2012, 8, 4989-5007.
- 37 Y. Zhang, S. Xia, L. Mikesell, N. Whisman, M. Fang, T. E. Steenwinkel, K. Chen, R. L. Luck, T. Werner and H. Liu, ACS Appl. Bio Mater., 2019, 2, 4986-4997.
- 38 C. Adamo and D. Jacquemin, Chem. Soc. Rev., 2013, 42, 845-856.

- 39 R. Dennington, T. A. Keith and J. M. Millam, Journal, GaussView, Version 6.0.16. Semichem Inc. 2016.
- 40 T. Yanai, D. Tew and N. Handy, Chem. Phys. Lett., 2004, 393, 51-57.
- 41 D. Jacquemin, E. A. Perpète, G. E. Scuseria, I. Ciofini and C. Adamo, J. Chem. Theory Comput., 2008, 4, 123-135.
- 42 S. Passarella, A. Schurr and P. Portincasa, Int. J. Mol. Sci., 2021, 22, 12620.
- 43 O. Murata, Y. Shindo, Y. Ikeda, N. Iwasawa, D. Citterio, K. Oka and Y. Hiruta, Anal. Chem., 2020, 92, 966-974.
- 44 A. Galaz, F. Cortes-Molina, R. Arce-Molina, I. Romero-Gomez, G. A. Mardones, L. F. Barros and A. San Martin, Anal. Chem., 2020, 92, 10643-10650.
- 45 Y. T. Zhang, M. L. Xing, H. H. Fang, W. D. Li, L. Wu and Z. P. Chen, Mol. Immunol., 2023, 154, 96-107.
- 46 M. J. Rogatzki, B. S. Ferguson, M. L. Goodwin and L. B. Gladden, Front. Neurosci., 2015, 9, 1-7.
- 47 B. Glancy, D. A. Kane, A. N. Kavazis, M. L. Goodwin, W. T. Willis and L. B. Gladden, J. Physiol., 2021, 599, 863-888.
- 48 A. Strachecka, M. Grzybek, A. A. Ptaszynska, A. Los, J. Chobotow and R. Rowinski, Biochemistry, 2019, 84, 435-440
- 49 A. Patgiri, O. S. Skinner, Y. Miyazaki, G. Schleifer, E. Marutani, H. Shah, R. Sharma, R. P. Goodman, T. L. To, X. R. Bao, F. Ichinose, W. M. Zapol and V. K. Mootha, Nat. Biotechnol., 2020, 38, 309.
- 50 D. Valenti, L. de Bari, A. Atlante and S. Passarella, Biochem. J., 2002, 364, 101-104.
- 51 N. Nemani, Z. W. Dong, C. C. Daw, T. R. Madaris, K. Ramachandran, B. T. Enslow, C. S. Rubannelsonkumar, Shanmughapriya, V. Mallireddigari, S. P. SinghMalla, K. Natarajanseenivasan, R. Hooper, C. E. Shannon, W. G. Tourtellotte, B. B. Singh, W. B. Reeves, K. Sharma, L. Norton, S. Srikantan, J. Soboloff and M. Madesh, Sci. Signal., 2020, 13, 1-14.
- 52 A. Giatromanolaki and A. L. Harris, Anticancer Res., 2001, 21, 4317-4324.
- 53 F. Arvelo and C. Cotte, Invest. Clin., 2009, 50, 529-546.
- 54 J. Peerlings, L. Van De Voorde, C. Mitea, R. Larue, A. Yaromina, S. Sandeleanu, L. Spiegelberg, L. Dubois, P. Lambin and F. M. Mottaghy, Methods, 2017, 130, 51-62.
- 55 J. P. Piret, D. Mottet, M. Raes and C. Michiels, in Cell Signaling, Transcription, and Translation as Therapeutic Targets, ed. M. Diederich, 2002, vol. 973, pp. 443-447.
- 56 Y. B. Zhang, X. L. Wang, E. A. Meister, K. R. Gong, S. C. Yan, G. W. Lu, X. M. Ji and G. Shao, Int. J. Mol. Sci., 2014, 15, 10999-11012.
- 57 N. K. Rana, P. Singh and B. Koch, Biol. Res., 2019, 52, 1-13.
- 58 B. H. Dingle, R. B. Rumble, M. C. Brouwers and E. Canc Care Ontarios Program, Can. J. Gastroenterol. Hepatol., 2005, 19, 711-716.
- 59 E. Ferrazzi and L. Stievano, Ann. Oncol., 2006, 17, V169-V172.
- 60 S. Dent, H. Messersmith and M. Trudeau, Breast Cancer Res. Treat., 2008, 108, 319-331.

- 61 N. Silvestris, S. Cinieri, I. La Torre, G. Pezzella, G. Numico, L. Orlando and V. Lorusso, Breast, 2008, 17, 220-226.
- 62 F. Fiteni, T. Nguyen, D. Vernerey, M. J. Paillard, S. Kim, M. Demarchi, F. Fein, C. Borg, F. Bonnetain and X. Pivot, Cancer Med., 2014, 3, 1502-1511.
- 63 T. Berg, T. J. Nottrup and H. Roed, Gynecol. Oncol., 2019, **155**, 530-537.
- 64 D. F. S. Kehrer, O. Soepenberg, W. J. Loos, J. Verweij and A. Sparreboom, Anti-Cancer Drugs, 2001, 12, 89–105.
- 65 R. W. Driver and L. X. Yang, Mini-Rev. Med. Chem., 2005, 5, 425-439.
- 66 D. Sriram, P. Yogeeswari, R. Thirumurugan and T. R. Bal, Nat. Prod. Res., 2005, 19, 393-412.
- 67 E. D. Chazin, R. D. Reis, W. T. Vellasco, L. F. E. Moor and T. R. A. Vasconcelos, Mini-Rev. Med. Chem., 2014, 14, 953-962.
- 68 S. A. Amin, N. Adhikari, T. Jha and S. Gayen, Anticancer Agents Med. Chem., 2018, 18, 1796-1814.
- 69 Q. Y. Ruan, G. Patel, J. Y. Wang, E. H. Luo, W. Zhou, E. Sieniawska, X. L. Hao and G. Y. Kai, Food Chem. Toxicol., 2021, 151, 112113.
- 70 P. T. Jain, F. A. Fornari, J. K. Randolph, M. S. Orr and D. A. Gewirtz, Biochem. Pharmacol., 1998, 55, 1263-1269.
- 71 R. Sakasai, H. Teraoka and R. S. Tibbetts, DNA Repair, 2010, 9, 76-82.
- 72 C. Mei, L. Lei, L. M. Tan, X. J. Xu, B. M. He, C. Luo, J. Y. Yin, X. Li, W. Zhang, H. H. Zhou and Z. Q. Liu, Biomed. Pharmacother., 2020, 125, 109875.
- 73 P. Jiang, W. J. Du and M. A. Wu, Protein Cell, 2014, 5, 592-602.
- 74 E. S. Cho, Y. H. Cha, H. S. Kim, N. H. Kim and J. I. Yook, Biomol. Ther., 2018, 26, 29-38.
- 75 T. X. Ge, J. W. Yang, S. H. Zhou, Y. C. Wang, Y. K. Li and X. M. Tong, Front. Endocrinol., 2020, 11, 1-11.
- 76 B. Stordal, N. Pavlakis and R. Davey, Cancer Treat. Rev., 2007, 33, 347-357.
- 77 F. Montagnani, G. Turrisi, C. Marinozzi, C. Aliberti and G. Fiorentini, Gastric Cancer, 2011, 14, 50-55.
- 78 F. Liang, S. Zhang, H. X. Xue and Q. Chen, BMC Cancer, 2017, 17, 871.
- 79 E. Jafarzadeh, V. Montazeri, S. Aliebrahimi, A. H. Sezavar, M. H. Ghahremani and S. N. Ostad, Life Sci., 2022, 304.
- 80 M. Pourmadadi, M. M. Eshaghi, E. Rahmani, N. Ajalli, S. Bakhshi, H. Mirkhaef, M. V. Lasemi, A. Rahdar, R. Behzadmehr and A. M. Diez-Pascual, J. Drug Delivery Sci. Technol., 2022, 77, 103928.
- 81 R. Ranasinghe, M. L. Mathai and A. Zulli, Heliyon, 2022, 8, E10608.
- 82 S. Oka, C. P. Hsu and J. Sadoshima, Circ. Res., 2012, 111, 611-627.
- 83 P. Wang, Y. Song, L. X. Zhang, H. P. He and X. Zhou, Curr. Med. Chem., 2005, 12, 2893-2913.
- 84 R. J. Browning, P. J. T. Reardon, M. Parhizkar, R. B. Pedley, M. Edirisinghe, J. C. Knowles and E. Stride, ACS Nano, 2017, 11, 8560-8578.